Prandtl number effects on extreme mixing events in forced stratified turbulence

Nicolaos Petropoulos[1],†**, Miles M.P. Couchman**[2]**, Ali Mashayek**[3]**,
Stephen M. de Bruyn Kops**[4] **and Colm-cille P. Caulfield**[1,5]

[1]Department of Applied Mathematics and Theoretical Physics, University of Cambridge, Cambridge CB3 0WA, UK

[2]Department of Mathematics and Statistics, York University, Toronto, ON M3J 1P3, Canada

[3]Department of Earth Sciences, University of Cambridge, Cambridge CB2 3EQ, UK

[4]Department of Mechanical and Industrial Engineering, University of Massachusetts Amherst, Amherst, MA 01003, USA

[5]Institute for Energy and Environmental Flows, University of Cambridge, Cambridge CB3 0EZ, UK

Relatively strongly stratified turbulent flows tend to self-organise into a 'layered anisotropic stratified turbulence' (LAST) regime, characterised by relatively deep and well-mixed density 'layers' separated by relatively thin 'interfaces' of enhanced density gradient. Understanding the associated mixing dynamics is a central problem in geophysical fluid dynamics. It is challenging to study LAST mixing, as it is associated with Reynolds numbers $Re := UL/\nu \gg 1$ and Froude numbers $Fr := (2\pi U)/(LN) \ll 1$ (U and L being characteristic velocity and length scales, ν the kinematic viscosity and N the buoyancy frequency). Since a sufficiently large dynamic range (largely) unaffected by stratification and viscosity is required, it is also necessary for the buoyancy Reynolds number $Re_b := \epsilon/(\nu N^2) \gg 1$, where ϵ is the (appropriately volume-averaged) turbulent kinetic energy dissipation rate. This requirement is exacerbated for oceanically relevant flows, as the Prandtl number $Pr := \nu/\kappa = O(10)$ in thermally stratified water (where κ is the thermal diffusivity), thus leading (potentially) to even finer density field structures. We report here on four forced fully resolved direct numerical simulations of stratified turbulence at various Froude ($Fr = 0.5, 2$) and Prandtl ($Pr = 1, 7$) numbers forced so that $Re_b = 50$, with resolutions up to $30\,240 \times 30\,240 \times 3780$. We find that, as Pr increases, emergent 'interfaces' become finer and their contribution to bulk mixing characteristics decreases at the expense of the small-scale density structures populating the well-mixed 'layers'. However, extreme mixing events (as quantified by significantly elevated local

† Email address for correspondence: np546@cam.ac.uk

destruction rates of buoyancy variance χ_0) are always preferentially found in the (statically stable) interfaces, irrespective of the value of Pr.

Key words: turbulent mixing, stratified turbulence, turbulence simulation

1. Introduction

In density-stratified flows, small-scale turbulence is known to enhance the rate at which density gradients are irreversibly smoothed by diffusive processes (i.e. mixed) and quantifying this rate in geophysical, environmental and industrial settings is of crucial importance. For instance, turbulent mixing is known to have a leading-order impact on global oceanic circulations (Wunsch & Ferrari 2004). Stratified turbulent flows are characterised by a variety of length scales associated with the structure of the turbulent velocity and density fields. Velocity fluctuations are smoothed by molecular viscosity and dissipated into heat below the Kolmogorov scale $L_K := (\nu^3/\epsilon)^{1/4}$ (where ν is the molecular viscosity and ϵ is the appropriately volume-averaged dissipation rate of turbulent kinetic energy). Similarly, density fluctuations are dissipated by molecular diffusion below the Batchelor scale $L_\rho := (\nu\kappa^2/\epsilon)^{1/4}$, κ being the molecular diffusivity. The (molecular) Prandtl number $Pr := \nu/\kappa$, that effectively quantifies the relative strength of viscous dissipation to diffusion, is the ratio of the square of these two length scales. Unlike the atmosphere, in which $Pr \simeq 0.7$ ($L_K \approx L_\rho$), in the ocean $Pr \sim O(10)$ when thermally stratified and the equivalent Schmidt number $Sc := \nu/D \sim O(1000)$ (D being the salt diffusivity) when dominantly salt-stratified.

For turbulent flows with $Pr \gg 1$, the inevitable scale separation with $L_\rho \ll L_K$ is such that fully resolved numerical simulations are highly challenging. However, there is increasing evidence indicating that the value of Pr has (perhaps unsurprisingly) a leading-order impact on irreversible scalar-mixing properties of stratified turbulent flows. For instance, the effects of Pr variations on the properties of secondary instabilities arising from the breakdown of Kelvin–Helmholtz billows were reported by Mashayek & Peltier (2011) and Salehipour, Peltier & Mashayek (2015). Similarly, Zhou, Taylor & Caulfield (2017) studied the influence of Pr variations on fully developed turbulence in stratified plane Couette flows using direct numerical simulations (DNS) and reported significant effects on density and momentum fluxes. Also using DNS, Legaspi & Waite (2020) analysed the effects of Pr variations on homogeneous forced stratified turbulence and showed, at least for the range of parameters they considered, that the $Pr = 1$ simulations are able to describe $Pr > 1$ dynamics at large scales and also that kinetic energy spectra (which importantly do not directly contain information from the density field) are largely unaffected by variations in Pr. However, they did observe Pr effects at small scales below L_K and in the density flux spectra. Therefore, here we focus on the influence of Pr variations on small-scale structures of the density field and their associated effects on the mixing properties of forced stratified turbulent flows.

Another important length scale associated with stratified turbulent flows is the buoyancy length scale $L_B := 2\pi U/N_0$, where U is a characteristic velocity of the flow and N_0 is a characteristic (background) value of the buoyancy frequency. Scaled using a characteristic horizontal length scale L_h, this parameter then defines a horizontal Froude number $Fr_h := L_B/L_h = 2\pi U/N_0 L_h$ that quantifies the relative strength of the stratification of the flow. For small horizontal Froude numbers Fr_h (i.e. relatively strongly stratified flows), the density field is known to self-organise into relatively well-mixed 'layers' (whose size scales as L_B; the buoyancy scale can therefore be thought of as the largest

energetically possible overturn) separated by relatively thin 'interfaces' of enhanced density gradient (Billant & Chomaz 2001; Waite 2011). Such density 'staircase' structure has important implications for irreversible scalar mixing in density-stratified turbulent flows. Couchman, de Bruyn Kops & Caulfield (2023) showed that (in the $Pr = 1$ case) while static instabilities are most prevalent within the well-mixed layers (that are hence characterised by relatively high values of ϵ), much of the scalar mixing, as described by the (appropriately volume-averaged) buoyancy variance destruction rate χ, is located in the relatively strongly stratified interfaces, a phenomenon that is not apparent when considering ϵ only. Hence, we focus here on the contribution of the different structures described above to the overall mixing properties of the flow, as described by χ. Note that we focus in this work on χ to describe mixing since this microstructure measurement currently provides the best observational means of probing ocean mixing (Gregg *et al.* 2018). Other quantities are also used in practical settings, such as buoyancy fluxes or turbulent diffusivities. However, these quantities usually rely upon some kind of averaging or parametrisation and our goal in this work is to probe the small-scale 'raw' structures of the density field and their contribution to mixing.

Fundamentally, we aim to understand how the density field's small-scale organisation shapes the bulk mixing properties of forced stratified turbulent flows at different Prandtl numbers. To this end, we analyse fully resolved DNS data of forced stratified turbulent flows at $Pr = 1$ and $Pr = 7$, each with $Fr = 0.5$ and $Fr = 2$, for values of Re such that the emergent $Re_b = 50$. The rest of this paper is organised as follows. We describe the DNS data in § 2 and then present the methodology used to extract distinct classes of density field structures in § 3. In § 4, we apply this methodology to the DNS data to segment the density field into weakly and strongly stratified interfaces, relatively small-scale 'lamella-like' structures and larger-scale density inversions and analyse the associated mixing properties of the extracted density structures. Brief conclusions are drawn in § 5.

2. Summary of the DNS datasets

We consider statistically steady, forced, fully resolved DNS of stratified turbulence from the simulation campaign originally reported by Almalkie & de Bruyn Kops (2012). The non-hydrostatic dimensionless Navier–Stokes equations under the Boussinesq approximation,

$$\left.\begin{aligned} \partial_t \boldsymbol{u} + \boldsymbol{u} \cdot \nabla \boldsymbol{u} = -\nabla p + \frac{1}{Re}\nabla^2 \boldsymbol{u} - \left(\frac{2\pi}{Fr}\right)^2 \rho \hat{\boldsymbol{z}} + \mathcal{F}, \quad \nabla \cdot \boldsymbol{u} = 0, \\ \partial_t \rho + \boldsymbol{u} \cdot \nabla \rho = \frac{1}{Pr\,Re}\nabla^2 \rho, \end{aligned}\right\} \quad (2.1)$$

are numerically integrated using a pseudospectral code in a triply periodic domain, where $\hat{\boldsymbol{z}}$ is the (upward) vertical unit vector. The dimensionless parameters are: the above-defined Prandtl number Pr; the Froude number $Fr := 2\pi U/(N_0 L)$ (where U and L are characteristic velocity and length scales associated with the forcing and N_0 is the background buoyancy frequency); and the Reynolds number $Re := UL/\nu$. The forcing term $\mathcal{F}$ corresponds to the deterministic 'Rf' scheme described in Rao & de Bruyn Kops (2011) and is designed to match a target low-wavenumber kinetic energy spectrum at steady state. This ensures a buoyancy Reynolds number $Re_b := \epsilon/(\nu N_0^2) \simeq 50$ for these simulations, where ϵ is the volume average of the point-wise local dissipation rate of turbulent kinetic energy ϵ_0, defined in terms of the symmetric part of the strain-rate tensor

s_{ij} as

$$\epsilon_0 := \frac{2}{Re} s_{ij} s_{ij}; \quad s_{ij} := \frac{1}{2}\left(\frac{\partial u_i}{\partial x_j} + \frac{\partial u_j}{\partial x_i}\right). \tag{2.2}$$

The density field is a superposition of a background linear density field $\bar{\rho}(z)$, characterised by a reference density ρ_0 and reference density gradient $-N_0^2\rho_0/g$, and a perturbation $\rho'(\boldsymbol{x}, t)$ so that, in dimensional form,

$$\rho(\boldsymbol{x}, t) = \bar{\rho}(z) + \rho'(\boldsymbol{x}, t) := \rho_0(1 - N_0^2 z/g) + \rho'(\boldsymbol{x}, t). \tag{2.3}$$

We can use ρ' to compute the (dimensional) local destruction rate of buoyancy variance:

$$\chi_0 := \frac{g^2 \kappa}{\rho_0^2 N_0^2} \boldsymbol{\nabla}\rho' \cdot \boldsymbol{\nabla}\rho'. \tag{2.4}$$

This quantity, appropriately scaled in this way by $-\rho_0 N_0^2/g$ (i.e. the density gradient against which the turbulence acts), corresponds to the local destruction rate of available potential energy (density) and can therefore be used as a proxy of local irreversible mixing (Howland, Taylor & Caulfield 2021) which can still be calculated pointwise-locally in the flow domain. Henceforth, we consider dimensionless quantities (the prefactor being $1/(Pr\,Re)$ in our system) and denote by χ the volume average of local χ_0 across the entire computational domain.

Here, we consider two values of the Prandtl number ($Pr = \{1, 7\}$) as well as two values of the Froude number ($Fr = \{0.5, 2\}$). The simulation parameters are summarised in table 1. We choose a grid spacing $\Delta \lesssim L_\rho$, and a vertical domain dimension of approximately $1.5L_B$. We consider a single snapshot in time (at statistical steady state) of the various simulations.

For the weakly stratified $Fr = 2$ simulations, a patch of elevated turbulence, described by relatively high values of the local dissipation rate ϵ_0, is generated by a large-scale vertically aligned vortex such as that reported in Couchman *et al.* (2023) for the P1F200 dataset (see figure 1). Outside the vortex, the density field self-organises into well-mixed layers separated by interfaces characterised by enhanced density gradients (see figures 2 and 3). In the strongly stratified $Fr = 0.5$ case, the vortex does not appear. Couchman *et al.* (2023) showed (at least for the P1F200 simulation) that the interfaces account for relatively large values of χ_0 and low values of ϵ_0 and hence 'extreme' values of the (local) flux coefficient $\Gamma_0 := \chi_0/\epsilon_0$, whereas the well-mixed layers were potentially more turbulent (relatively large values of ϵ_0) but characterised by relatively low values of χ_0 (owing to relatively low values of the density gradient) and hence relatively low values of Γ_0. Here we aim to understand whether such a picture holds for flows with different values of Fr and more importantly of Pr, and to understand how different structures in the density field (defined more precisely in the next section) influence the mixing within the flow, quantified by values of (local) χ_0.

3. Density field segmentation methodology

Following Couchman *et al.* (2023), we are interested in the contribution to mixing of the emergent stably stratified interfaces appearing in the density field and how this contribution varies as a function of Pr and Fr. As Pr increases, we expect finer structures to arise in the intervening well-mixed regions and we also are interested in understanding how these structures shape the mixing properties of the flow. Therefore, prior to any analysis, the flow is segmented into four different categories based on the local (vertical) density

Name	Pr	Fr	Re	Re_λ	Domain size	Grid size	L_K	L_T	L_B	ϵ	χ
P1F200	1	2	1717	184	$2\pi \times 2\pi \times \pi$	$4096 \times 4096 \times 2048$	0.0037	0.099	1.99	1.05	0.54
P1F050	1	0.5	24 096	826	$2\pi \times 2\pi \times \pi/4$	$11\,264 \times 11\,264 \times 1408$	0.00052	0.030	0.52	0.95	0.38
P7F200	7	2	1717	178	$2\pi \times 2\pi \times \pi$	$6144 \times 6144 \times 3072$	0.0037	0.096	1.95	1.09	0.44
P7F050	7	0.5	24 096	655	$2\pi \times 2\pi \times \pi/4$	$30\,240 \times 30\,240 \times 3780$	0.00048	0.024	0.51	1.36	0.43

Table 1. Summary of the DNS data. Parameters L_K, L_T and L_B denote the Kolmogorov, Taylor and buoyancy scales.

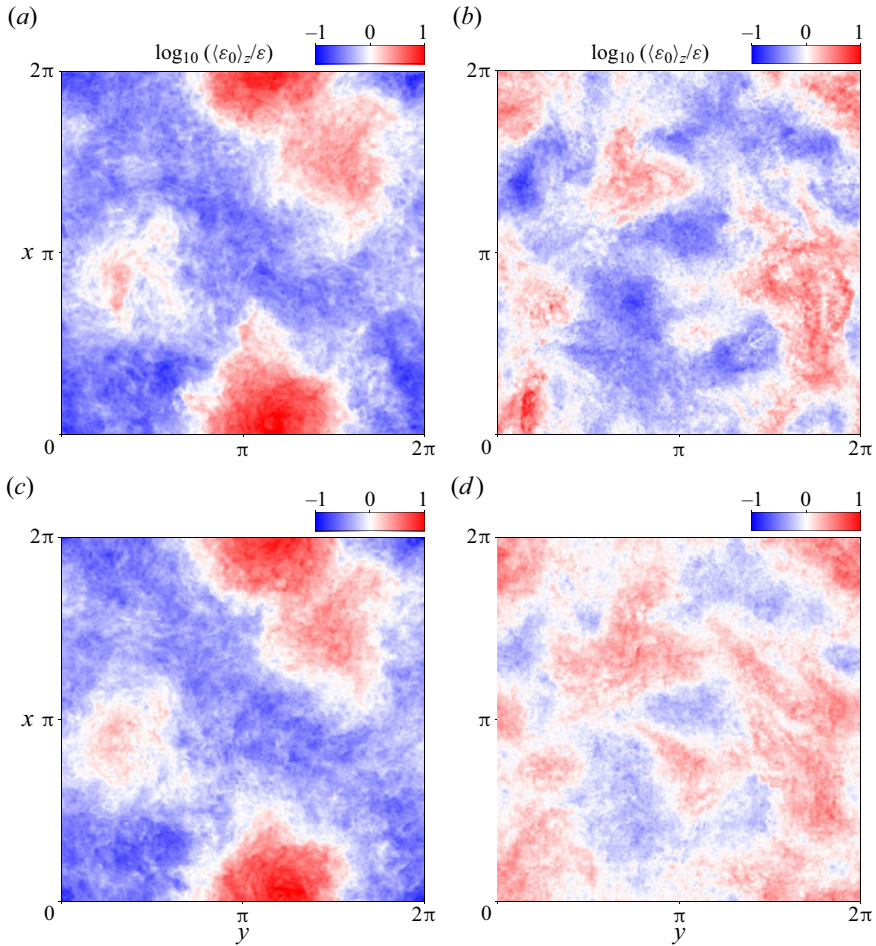Figure 1. Vertical average of the dissipation rate of turbulent kinetic energy $\langle \epsilon_0 \rangle_z$ (scaled by the bulk average ϵ) in the horizontal x–y plane for the (*a*) P1F200, (*b*) P1F050, (*c*) P7F200 and (*d*) P7F050 simulations. A coherent patch of elevated dissipation rate is found in the $Fr = 2$ simulations (corresponding to a large-scale vortex; see Couchman *et al.* (2023) for more details). This vortex is not sustained in the strongly stratified case $F = 0.5$.

gradient $\partial_z \rho$ as well as the neighbouring (vertical) structure of the flow. We apply the following methodology, as summarised in figure 2:

(i) Stably stratified interfaces. We sort vertical density profiles by values of the density ρ in order to create statically stable density profiles $\rho^*(x)$. We identify points of the dataset whose values of the density remain unaltered by the sorting procedure, i.e. points that satisfy $\rho(x) = \rho^*(x)$. These points are by definition statically stable and have relatively high values of the background buoyancy gradient $N_*^2 :=$ $-g/(\rho_0 N_0^2)\partial_z \rho^*$ (see figure 2*b–d*) and correspond to stably stratified interfaces lying between relatively well-mixed regions, such as those reported by Couchman *et al.* (2023) for the P1F200 dataset. We thus refer to such points as belonging to the **INT** ('interface') cluster, which is further subdivided into relatively strongly stratified (**SINT**) and relatively weakly stratified (**WINT**) interfaces, for $N_*^2 > 1$ and $N_*^2 \leq 1$ respectively.
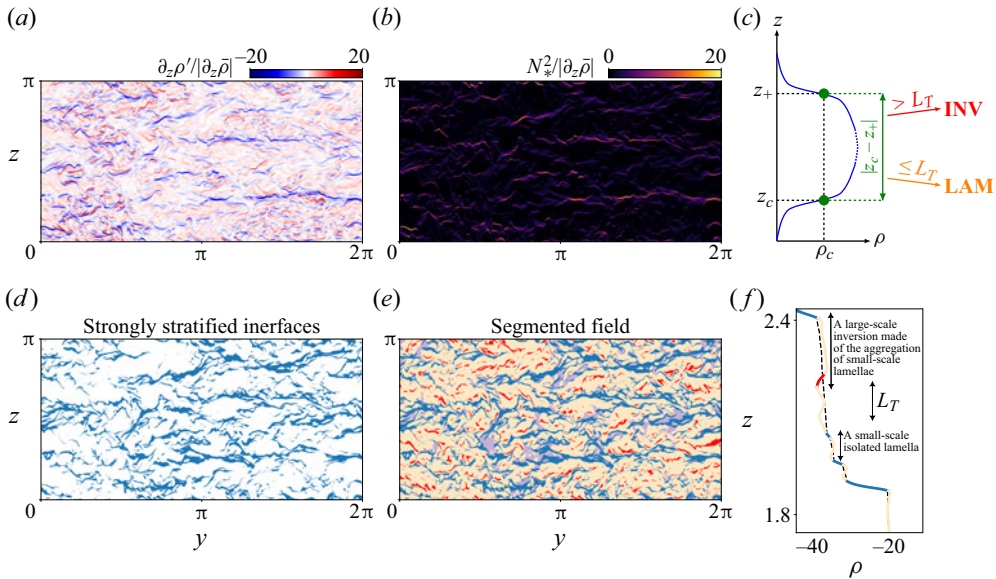
Figure 2. Flow segmentation methodology. For the P1F200 simulation, the density field, represented here by its vertical gradient as shown in (*a*), is vertically sorted into a statically stable field, whose vertical gradient is denoted N_*^2 (up to a multiplicative constant), as shown in (*b*). The sorting algorithm highlights the stable interfaces of the density field, i.e. the points of the density field unaltered by the sorting procedure. The strongly stratified interfaces (**SINT**, in blue with $N_*^2 > 1$) are then extracted in (*d*). The entire segmented field is shown in (*e*), including the weakly stratified interfaces with $N_*^2 \leq 1$ (**WINT**, in purple), and the relatively well-mixed regions between interfaces, further subdivided into small-scale 'lamella' structures (**LAM**, in orange) and larger-scale density inversions (**INV**, in red) using the procedure described in § 3 and shown schematically in (*c*), based on the Taylor microscale L_T. A segmented vertical profile is presented in (*f*), showing strongly stratified interfaces (in blue) separating relatively well-mixed regions made up of isolated lamellae, aggregated ones as well as a large-scale inversion. The dashed line corresponds to the sorted density field ρ^*. Note that because of the segmentation algorithm used in this work, only the unstable (strongly stratified in absolute value) edge of the large-scale density inversion is considered in the **INV** cluster, the rest of the inversion being made of smaller-scale aggregating lamellae. This edge corresponds to the maximal density gradient found in the inversion, suggesting a large contribution to statistics of χ_0, as shown in § 4 and as suggested experimentally (see, for instance, Hult, Troy & Koseff 2011).

(ii) Relatively well-mixed layers. We subdivide points that are altered by the sorting procedure (i.e. are not within an interface **INT**) into two categories depending on the local density gradient $\partial_z \rho$ and neighbouring structure of the (unsorted) density field ρ, in particular relative to L_T, the Taylor microscale of the flow. Parameter L_T describes the scale at which viscosity starts to affect the development of turbulent eddies significantly, defined (dimensionally) as $L_T := \sqrt{10\nu\mathcal{K}/\epsilon}$, where $\mathcal{K}$ is the volume-averaged turbulent kinetic energy. As illustrated in figure 2(*c*), by considering a point in the dataset at vertical coordinate z_c with associated density $\rho_c := \rho(z_c)$ satisfying $\partial_z \rho(z_c) > 0$, we define z_+ as the closest point moving upwards for which $\rho(z_+) = \rho_c$. As equality is difficult to ensure numerically, we define

$$z_+ := \min\{z > z_c \mid \rho(z) \leq \rho(z_c)\}. \tag{3.1}$$

Similarly, if $\partial_z \rho(z_c) < 0$, we define $z_- := \min\{z < z_c \mid \rho(z) \geq \rho(z_c)\}$. If $|z_c - z_+| \leq L_T$ (or $|z_c - z_-| \leq L_T$ depending on the local value of the density gradient), we have identified a relatively small-scale structure in the density field, such as a

983 R1-7

blob or stretched 'lamella' as discussed in detail by Villermaux (2019), which is strongly affected by viscosity. Therefore we classify these structures as belonging to the **LAM** ('lamella') cluster. Conversely, if $|z_c - z_+| > L_T$ (or $|z_c - z_-| > L_T$), we have identified a point belonging to a relatively large-scale density inversion largely unaffected by viscosity, and so we classify it as being in the **INV** ('inversion') cluster. This algorithm is applied to all vertical levels z_c in a given vertical profile of a simulation, and then for all the profiles in the simulation box. Note that the well-mixed regions can be made up of many 'aggregating' lamellae, hence the large vertical extent of the **LAM** cluster (even though this cluster is made up of relatively thin density structures). Similarly, because of the segmentation algorithm used in this work, only the edges of large-scale density inversions are considered in the **INV** cluster, the bulk of the inversion being made of smaller-scale (aggregating) lamellae. (Indeed, if z_c and $z_\pm$ are separated by a distance larger than L_T, only the point z_c will be considered in **INV** but not all the points between z_c and $z_\pm$, these points being perhaps part of smaller-scale structures.) These edges correspond to the region of maximal (vertical) density gradient in the inversion and hence to the maximal contribution to the statistics of χ_0 within the inversion (as is shown in § 4; this fact has also been demonstrated experimentally – see Hult *et al.* (2011) for instance), motivating further our choice of clusters. Note that the small-scale structure of the relatively well-mixed regions is potentially a consequence of the breakdown of various instabilities, such as the Kelvin–Helmholtz one. Because we are considering only one snapshot in time (at statistical steady state), we cannot further check this hypothesis.

This segmentation methodology, summarised in figure 2, is applied to the four datasets considered in this work, as shown in figure 3.

4. Cluster properties

4.1. *Contributions to* χ

We consider the relative importance of each cluster defined in § 3 in terms of their contribution to the local and bulk mixing properties of the flow, as described by local χ_0 and volume-averaged χ. We particularly focus on the role of 'extreme' mixing events and therefore sort the data by decreasing values of χ_0, defining a sorted vector $\boldsymbol{\chi}_0^* = (\chi_0^{0*}, \ldots, \chi_0^{M*})$, where M is the number of points in the dataset and χ_0^{0*} and χ_0^{M*} are the greatest and lowest values of χ_0 found in the dataset, respectively. This vector can be used to construct the normalised cumulative contribution to χ as

$$\forall n \in \{1, \ldots, M\}, \quad \chi^c(n) := \frac{1}{\chi} \sum_{i=1}^{n} \chi_0^{i*}. \tag{4.1}$$

The cumulative contribution χ^c is plotted in figure 4 for each dataset (solid black line), highlighting the fact that the dominant contribution to χ is generated by a relatively small set of localised 'extreme' events, regardless of *Fr* and *Pr*. More specifically, for the four sets of parameters considered in this work, approximately 80 % of the contribution to χ is contained within the first 10 % of the points sorted by decreasing values of χ_0 (and hence 10 % of the box volume). Similar statistics are observed in oceanographic data (Couchman *et al.* 2021).

The total contribution of each cluster to bulk χ is shown in figure 4(*e*). We also assign the data points sorted by values of χ_0 into $n = 20$ equal-volume bins, in order
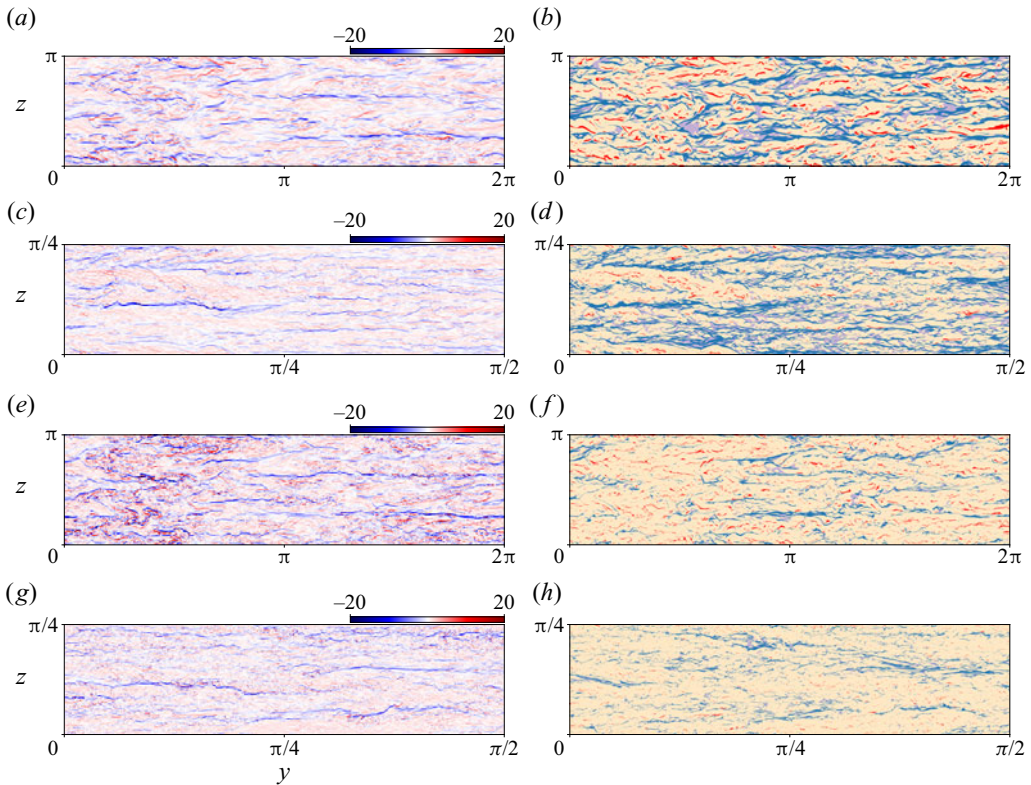
Figure 3. Normalised vertical density gradient $\partial_z \rho' / |\partial_z \bar{\rho}|$ (a,c,e,g) and associated segmented fields (b,d,f,h), for simulations P1F200 (a,b), P1F050 (c,d), P7F200 (e,f) and P7F050 (g,h). The strongly stratified interfaces (**SINT**) are depicted in blue, the small-scale structures (**LAM**) in orange, the larger-scale density inversions (**INV**) in red and the weakly stably stratified regions (**WINT**) in purple.

to calculate a relative contribution of points in each cluster to the bin-volume-averaged $\langle \chi \rangle_{bin} := \sum_{bin} \chi_0 / (V/n)$, where V is the total number of points in the domain, as illustrated by coloured shading in figure 4(a–d). Focusing on the $Pr = 1$ case, the contribution (figure 4e) from the strongly stratified interfaces (**SINT** cluster) to bulk χ is roughly 25 %–35 %, whereas the contribution from small-scale structures (**LAM**) reaches ∼60 %. As Fr decreases and stratification strengthens, the total contribution from large-scale inversions (**INV**) shrinks from ∼10 % for $Fr = 2$ to less than 3 % for $Fr = 0.5$, possibly due to the suppression of large-scale overturnings by relatively strong stratification. We observe similar trends for the relative contributions in each bin. In increasing the Prandtl number from $Pr = 1$ to 7, strong interfaces become (perhaps unsurprisingly) finer (figure 3f,h) and their total contribution shrinks to about 10 %, whereas the total contribution from small-scale structures in 'lamella' (**LAM**) increases to about 80 %–90 %. The total contribution from large-scale inversions does not exceed 10 %. Again, we observe similar trends in the relative contributions as χ_0 decreases.

4.2. *Statistics of Γ*

For each bin in figure 4, we compute a mean value of the (local) flux coefficient $\Gamma_0 := \chi_0 / \epsilon_0$ associated with each cluster (see dashed lines), although such mean values
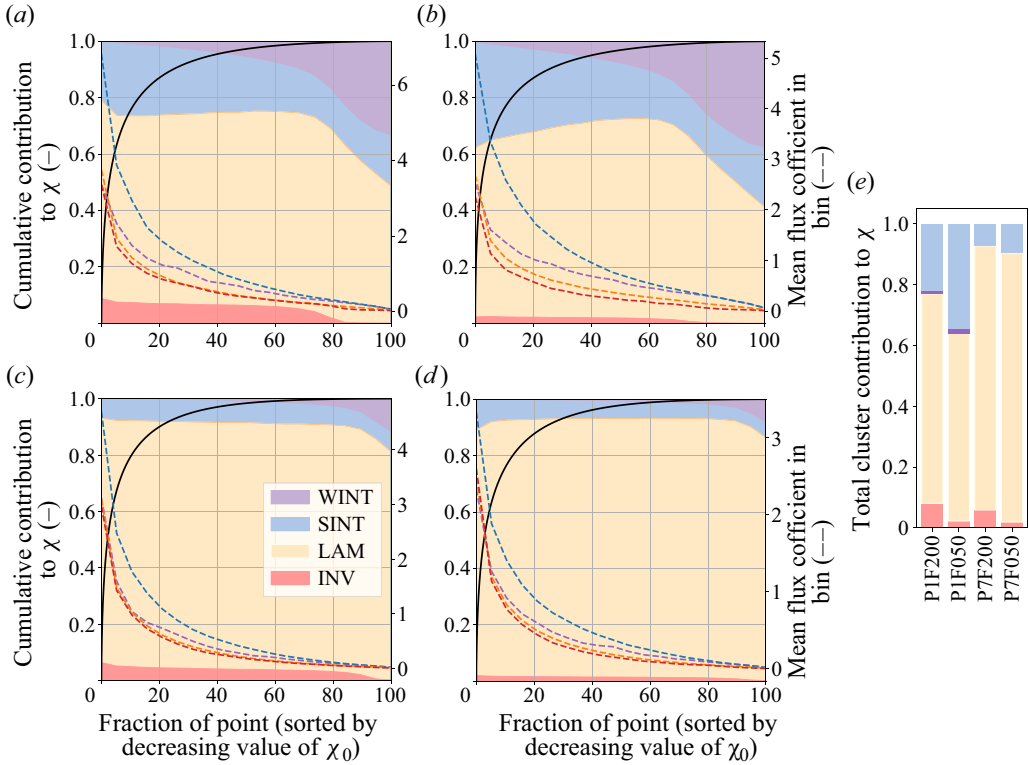
Figure 4. Normalised cumulative contribution to χ (black line; see (4.1)) for each simulation: (*a*) P1F200, (*b*) P1F050, (*c*) P7F200 and (*d*) P7F050. Data points are assigned to 20 equal-volume bins, sorted by decreasing χ_0 and clustered using the method presented in § 3. For each bin, we compute the relative contribution of each cluster to $\langle \chi \rangle_{bin}$, as shown by the heights of the coloured regions. For each bin, we compute the (arithmetic) mean value of $\Gamma_0 := \chi_0/\epsilon_0$ for each cluster (dashed lines). (*e*) Total contributions to χ from each cluster for the four simulations.

of ratios of local quantities should always be treated with caution. The leftmost bins (corresponding to the most 'extreme' values of χ_0) have the largest values of Γ_0 (of order unity, significantly above the canonical value $\Gamma = 0.2$) suggesting strongly that the extreme mixing events (large χ_0) are not necessarily correlated with extreme dissipation events (large ϵ_0). Among the extreme events in χ_0, those in the strongly stratified interfaces (**SINT**) cluster correspond to the largest mean values of Γ_0 (as suggested by Couchman *et al.* (2023) for the $Pr = 1$, $Fr = 2$ case), independently of variations in Pr and Fr. This point is further emphasised in figure 5 where we plot the probability density functions (p.d.f.s) of $\log_{10}(\chi_0)$, $\log_{10}(\epsilon_0)$ and $\log_{10}(\Gamma_0)$ for the different clusters and simulations (computed using normalised histograms with 50 equispaced bins). We also present the statistical mean of χ_0, ϵ_0 and Γ_0 (computed using normalised histograms with 50 bins in log-space). Interestingly, the χ_0 distributions are skewed towards high values (note that this skewness seems exacerbated for the **INV** cluster, for reasons presented in § 3) and the Γ_0 ones encompass almost four orders of magnitude, emphasising again the fact that extreme local values of χ_0 are important in setting the overall mixing statistics. Note that these statistics are computed using all the data points in the simulation boxes and hence all the resolved length scales. In more practical settings, where all the length scales down to the Batchelor scales are not necessarily accessible, these p.d.f.s might sharpen
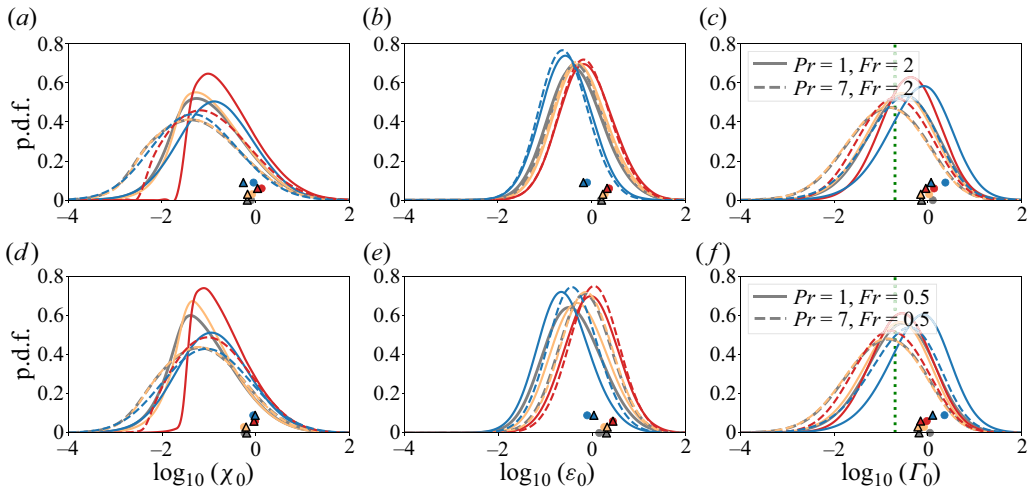
983 R1-10

Figure 5. The p.d.f.s for $\log_{10}(\chi_0)$ (a,d), $\log_{10}(\epsilon_0)$ (b,e) and $\log_{10}(\Gamma_0)$ (c,f) for the different clusters defined in § 3 and for the four simulations. The statistical mean of each field (without the logarithm) is represented by a colour-coded circle ($Pr = 1$) or triangle ($Pr = 7$). The green dotted vertical line corresponds to the canonical value $\Gamma = 0.2$.

around their mean. However, the effective coarse-graining induced by the resolution of the measurements might smooth the fields and hence overlook the (very) thin but yet important strongly stratified interfaces (especially in the high-Prandtl-number case where these interfaces are extremely thin), potentially leading to undersampling of important regions of the density field, and raising the important question of what is the relevant scale at which a turbulent density field should be profiled to get mixing statistics right. This question is not addressed here and is left for future work. For each simulation, the statistical mean of the flux coefficient Γ_0 is maximised for the strongly stratified interfaces (almost twice as large as the statistical mean for the entire dataset), because of relatively low values of ϵ_0 and large values of χ_0. As the Prandtl number increases, the statistical mean of Γ_0 decreases (a result also observed by Salehipour *et al.* (2015)) for both the weakly and strongly stratified cases, for the following (different) reasons.

In the weakly stratified simulations with $Fr = 2$ (figure 5a–c), density effectively acts as a passive scalar (as can be seen from the weakly stratified scaling of Riley, Metcalfe & Weissman (1981), for instance) and hence the statistics of ϵ_0 do not depend on Pr, as can be seen in figure 5(b). However, as Pr increases, the left-hand tails of the χ_0 distributions become more significant, as might be expected for the mixing of an effectively passive scalar, as χ_0 is multiplied by $(Pr\,Re)^{-1}$ where Re is fixed. We note that a widening of the tails of $\partial_z\rho'$ (not shown here; see for instance Riley, Couchman & de Bruyn Kops (2023)) effectively rebuilds the right-hand tail of χ_0, explaining why the p.d.f. of χ_0 is not just shifted toward lower values. A more in-depth discussion of this phenomenon is provided by Bragg & de Bruyn Kops (2023). As a result of the statistics of ϵ_0 remaining roughly independent of Pr but those of χ_0 decreasing with increasing Pr, the statistics of Γ_0 decrease as Pr increases for the weakly stratified ($Fr = 2$) case.

Conversely, in the strongly stratified simulations with $Fr = 0.5$, buoyancy acts 'actively' on the momentum field, as demonstrated for instance by the strongly stratified scaling analysis of Billant & Chomaz (2001). Moreover, as Pr increases, the volume contribution of the small-scale structures (**LAM** cluster) increases at the expense of the strongly stratified interfaces (**SINT**) (see figure 4). The **LAM** structures, which locally are only

weakly affected by stratification because they populate the relatively well-mixed regions of the flow, are viscously affected (as their vertical extent is, by definition, smaller than L_T) but still significantly disordered. As a result, their local static instability inevitably encourages increased viscous dissipation, and so their enhanced prevalence actually shifts the statistics of ϵ_0 towards higher values for the $Pr = 7$ flows as compared with $Pr = 1$ (yellow curves, figure 5*f*). In this sense, enhanced stratification at higher Pr actually makes the flow 'more turbulent', reminiscent of the prediction by Pearson & Linden (1983) of relatively long-lived 'approximately horizontal striations' in high-Pr decaying stratified turbulence. Also, though this is a second-order effect, for the strongly stratified simulations the left-hand tail of the χ_0 distribution once again becomes somewhat more significant as Pr increases. We note that while the forcing scheme endeavours to maintain a constant Re_b, bulk ϵ is slightly mismatched between the two Pr simulations at $Fr = 0.5$ (see table 1). Therefore, while increased Pr dramatically changes the relative prevalence of **LAM** versus **SINT** structures, part of the observed increase in local ϵ_0 statistics at $Pr = 7$, $Fr = 0.5$ is due to the slight mismatch in targeted bulk ϵ rather than being a purely Pr effect. Importantly, it is apparent in figure 5(*e*) that the total amount of irreversible mixing for the flow with $Pr = 7$ actually slightly increases compared to $Pr = 1$ in the more strongly stratified $Fr = 0.5$ simulations, essentially because the $Pr = 7$ flow is more vigorous, despite the fact that Γ_0 appears to decrease with increasing Pr. Therefore, consideration of Γ_0, or even $\Gamma := \chi / \epsilon$ (constructed from volume-averaged dissipation rates), in isolation should be treated with caution.

5. Discussion

We have analysed the influence of the Prandtl number Pr and Froude number Fr on density structures in forced turbulent stratified flows and their contribution to irreversible scalar mixing properties. Using fully resolved DNS data and a flow segmentation algorithm based on the local value of the (vertical) density gradient and the local (vertical) structure of the density field, we have extracted distinct regions of the turbulent density field – interfaces (both relatively strong and relatively weak) separating well-mixed density layers made up of both small-scale lamellar structures and larger scale density inversions – and analysed their contribution to the bulk value of the destruction rate of buoyancy variance χ and to the statistics of the (locally evaluated) flux coefficient Γ_0.

As Pr increases, the strongly stratified density interfaces become finer and their contribution to average values of χ decreases at the expense of the small-scale lamellar structures in the relatively well-mixed density layers. However, similarly to the flow with $Pr = 1$ (Couchman *et al.* 2023), these structures are 'quiescent', yet mixing hotspots. The points in these structures associated with the largest values of (local) χ_0 are associated with extreme values of Γ_0 and hence with relatively low values of ϵ_0. More generally, the flux coefficient associated with strongly stratified structures is (in an averaged sense) essentially twice as large as its value for the three other segmented regions, regardless of the values of Pr and Fr. All in all, strongly stratified interfaces are therefore characterised by relatively large values of χ_0 and relatively weak values of ϵ_0 compared with the other density structures considered in this work and are therefore likely to be overlooked if considering ϵ_0 (or indeed the volume average ϵ) alone as a proxy for significant irreversible mixing.

As is becoming increasingly well appreciated, a universal value of Γ is not able to capture the complex and inhomogeneous structures of the density and density gradient turbulent fields. Moreover, our description of the density fields as well as consideration of the considered mixing regime (i.e. 'passive' mixing at higher Fr as compared with

'active' mixing at lower *Fr*) offers a potential explanation for the empirical observation that the 'mixing efficiency' $\Gamma/(1 + \Gamma)$ decreases with *Pr*. On the one hand, mixing in the relatively weakly stratified case can be described as 'passive': the velocity field and hence ϵ_0 are largely unaffected by *Pr* but the small-scale structure of the density field evolves as *Pr* increases from 1 to 7 in a way that results in a decrease in χ_0 and thus the flux coefficient Γ_0. On the other hand, mixing in the relatively strongly stratified case can be thought of as 'active', with the density field and its small-scale lamellar structure having a leading-order impact on the rate at which the turbulent kinetic energy is dissipated (ϵ_0), ultimately leading to a decrease in Γ_0 as *Pr* increases. This shows another way in which a focus on the flux coefficient can be misleading. Since the decrease in Γ_0 is actually principally related to an increase in ϵ_0, the total amount of mixing (quantified by χ) actually increases in the higher-*Pr*, strongly stratified flow considered here. Accurately predicting the flux coefficient being crucial to modelling mixing in large-scale ocean models for instance (through turbulent diffusivities for instance), our study emphasises the need to better understand the dependence of this parameter on the small-scale structure of the density field. Another key result of our analysis is that the Prandtl number *Pr* has a leading-order impact (at least compared with the Froude number *Fr*) on the density field structures and their mixing properties, further emphasising the need to take this parameter into account when 'measuring mixing', a process that is inherently a diffusive one (Villermaux 2019; Caulfield 2021) and that affects the density field.

We here considered steady-state forced stratified turbulent flows, and so it would now be interesting to apply our segmentation and associated mixing contribution analysis to time-dependent decaying stratified turbulent flows. For example, what is the fate of the different emerging structures? Can a separate analysis of the temporal evolution of each structure help us better understand the mixing history of a stratified turbulent flow as a whole and unveil the fundamental rules of stratified mixing? These are questions left for future work.

Declaration of interests. The authors report no conflict of interest.

Author ORCIDs.

Nicolaos Petropoulos https://orcid.org/0000-0002-8585-7139;

Miles M.P. Couchman https://orcid.org/0000-0002-4667-6829;

Ali Mashayek https://orcid.org/0000-0002-8202-3294;

Stephen M. de Bruyn Kops https://orcid.org/0000-0002-7727-8786;

Colm-cille P. Caulfield https://orcid.org/0000-0002-3170-9480.

REFERENCES

ALMALKIE, S. & DE BRUYN KOPS, S.M. 2012 Kinetic energy dynamics in forced, homogeneous, and axisymmetric stably stratified turbulence. *J. Turbul.* **13**, N29.

BILLANT, P. & CHOMAZ, J.-M. 2001 Self-similarity of strongly stratified inviscid flows. *Phys. Fluids* **13** (6), 1645–1651.

BRAGG, A.D. & DE BRUYN KOPS, S.M. 2023 Understanding the effect of Prandtl number on momentum and scalar mixing rates in neutral and stably stratified flows using gradient field dynamics. *J. Fluid Mech.* (submitted) arXiv:2308.00518.

CAULFIELD, C.P. 2021 Layering, instabilities, and mixing in turbulent stratified flows. *Annu. Rev. Fluid Mech.* **53** (1), 113–145.

COUCHMAN, M.M.P., DE BRUYN KOPS, S.M. & CAULFIELD, C.P. 2023 Mixing across stable density interfaces in forced stratified turbulence. *J. Fluid Mech.* **961**, A20.

COUCHMAN, M.M.P., WYNNE-CATTANACH, B., ALFORD, M.H., CAULFIELD, C.P., KERSWELL, R.R., MACKINNON, J.A. & VOET, G. 2021 Data-driven identification of turbulent oceanic mixing from observational microstructure data. *Geophys. Res. Lett.* **48** (23), e2021GL094978.

GREGG, M.C., D'ASARO, E.A., RILEY, J.J. & KUNZE, E. 2018 Mixing efficiency in the ocean. *Ann. Rev. Mar. Sci.* **10**, 443–473.

HOWLAND, C.J., TAYLOR, J.R. & CAULFIELD, C.P. 2021 Quantifying mixing and available potential energy in vertically periodic simulations of stratified flows. *J. Fluid Mech.* **914**, A12.

HULT, E.L., TROY, C.D. & KOSEFF, J.R. 2011 The mixing efficiency of interfacial waves breaking at a ridge. 2. Local mixing processes. *J. Geophys. Res.* **116**, C02004.

LEGASPI, J.D. & WAITE, M.L. 2020 Prandtl number dependence of stratified turbulence. *J. Fluid Mech.* **903**, A12.

MASHAYEK, A. & PELTIER, W.R. 2011 Turbulence transition in stratified atmospheric and oceanic shear flows: Reynolds and Prandtl number controls upon the mechanism. *Geophys. Res. Lett.* **38** (16), L16612.

PEARSON, H.J. & LINDEN, P.F. 1983 The final stage of decay of turbulence in stably stratified fluid. *J. Fluid Mech.* **134**, 195–203.

RAO, K.J. & DE BRUYN KOPS, S.M. 2011 A mathematical framework for forcing turbulence applied to horizontally homogeneous stratified flow. *Phys. Fluids* **23** (6), 065110.

RILEY, J.J., COUCHMAN, M.M.P. & DE BRUYN KOPS, S.M. 2023 The effect of Prandtl number on decaying stratified turbulence. *J. Turbul.* **24** (6–7), 330–348.

RILEY, J.J., METCALFE, R.W. & WEISSMAN, M.A. 1981 Direct numerical simulations of homogeneous turbulence in density-stratified fluids. In *AIP Conference Proceedings*, vol. 76, pp. 79–112. AIP Publishing.

SALEHIPOUR, H., PELTIER, W.R. & MASHAYEK, A. 2015 Turbulent diapycnal mixing in stratified shear flows: the influence of Prandtl number on mixing efficiency and transition at high Reynolds number. *J. Fluid Mech.* **773**, 178–223.

VILLERMAUX, E. 2019 Mixing versus stirring. *Annu. Rev. Fluid Mech.* **51**, 245–273.

WAITE, M.L. 2011 Stratified turbulence at the buoyancy scale. *Phys. Fluids* **23** (6), 066602.

WUNSCH, C. & FERRARI, R. 2004 Vertical mixing, energy, and the general circulation of the oceans. *Annu. Rev. Fluid Mech.* **36**, 281–314.

ZHOU, Q., TAYLOR, J.R. & CAULFIELD, C.P. 2017 Self-similar mixing in stratified plane Couette flow for varying Prandtl number. *J. Fluid Mech.* **820**, 86–120.